A single-phase elastic hyperbolic metamaterial with anisotropic mass density

R. Zhu,[1,a)] Y. Y. Chen,[1] Y. S. Wang,[2] G. K. Hu,[3] and G. L. Huang[1,b)]
[1]*Department of Mechanical and Aerospace Engineering, University of Missouri, Columbia, Missouri 65211, USA*
[2]*Institute of Engineering Mechanics, Beijing Jiaotong University, Beijing, People's Republic of China*
[3]*School of Aerospace Engineering, Beijing Institute of Technology, Beijing, People's Republic of China*

(Received 16 October 2015; revised 28 January 2016; accepted 27 February 2016; published online 30 June 2016)

Wave propagation can be manipulated at a deep subwavelength scale through the locally resonant metamaterial that possesses unusual effective material properties. Hyperlens due to metamaterial's anomalous anisotropy can lead to superior-resolution imaging. In this paper, a single-phase elastic metamaterial with strongly anisotropic effective mass density has been designed. The proposed metamaterial utilizes the independently adjustable locally resonant motions of the subwavelength-scale microstructures along the two principal directions. High anisotropy in the effective mass densities obtained by the numerical-based effective medium theory can be found and even have opposite signs. For practical applications, shunted piezoelectric elements are introduced into the microstructure to tailor the effective mass density in a broad frequency range. Finally, to validate the design, an elastic hyperlens made of the single-phase hyperbolic metamaterial is proposed with subwavelength longitudinal wave imaging illustrated numerically. The proposed single-phase hyperbolic metamaterial has many promising applications for high resolution damage imaging in nondestructive evaluation and structural health monitoring. © *2016 Acoustical Society of America*.
[http://dx.doi.org/10.1121/1.4950728]

[MRH] Pages: 3303–3310

I. INTRODUCTION

Metamaterials, with engineered subwavelength-scale microstructures, have exhibited many unique and useful abilities for wave control. Among them, super-resolution imaging is one of the most attractive abilities even since it was first discovered. Based on the negative index of refraction of electromagnetic (EM) metamaterials, Pendry[1] was the first to theoretically investigated super-resolution imaging by using the so-called "superlens," which has the ability of not only focusing the propagating waves but also amplifying the evanescent waves. Since the fine details of the imaging object corresponding to the high spatial frequency components are carried by the evanescent waves, imaging with resolution beyond the diffraction limit can be obtained by using superlens technology.[2] Inspired by Pendry's pioneering work, many superlens designs have been proposed not only for EM waves but also for acoustic waves.[3–8]

It is observed that the subwavelength images obtained by a superlens are typically limited to the near field of the lens due to the fact that it can only amplify the evanescent waves but not change their decaying behavior. A hyperlens, on the other hand, can not only carry the subwavelength information contained within the evanescent waves across the lens, but also magnify it, thereby converting it to propagating waves such that the information travels to the far-field outside the lens. Basically, the realization of the hyperlens for far-field super-resolution acoustic imaging relies on the elliptical or hyperbolic equifrequency contour (EFC) which allows for very high spatial frequency components carrying the detailed information from objects. Christensen *et al.*[9,10] designed an acoustic metamaterial formed by layers of perforated plates and experimentally demonstrated its hyperbolic dispersion and subwavelength acoustic imaging based on the anisotropic lattices of scatterers. Anisotropic dynamic mass density provides one of the most practical options to fulfill the material requirement of elliptical or hyperbolic EFC(Refs. 11–15). Li *et al.*[11] designed an acoustic metamaterial with strongly anisotropic mass density from alternating layers of brass fins and air. An acoustic hyperlens with elliptical EFC was fabricated by using the acoustic metamaterial and subwavelength acoustic images with a $\lambda/6.8 - \lambda/4.1$ resolution were experimentally obtained. Shen *et al.*[12] designed an acoustic hyperbolic metamaterial with the density being positive in one direction and negative in the orthogonal direction. Subwavelength imaging ($\lambda/4.7$) and partial focusing for acoustic waves was experimentally demonstrated in a broad frequency range.

Elastic metamaterials (EMMs), with properly designed locally resonant (LR) microstructures, can behave as effective materials with extraordinary material properties that are not found in nature, such as negative mass density,[16–18] negative elastic modulus,[19] and anisotropic mass density.[20–23] With the abnormal effective material properties, EMMs have been given unique subwavelength-scale wave manipulation abilities such as flat lens wave focusing,[24] 90-deg elastic wave bending,[25] and negative refractions.[26,27] Subwavelength imaging for elastic waves has also been investigated, although not as

[a)]Present address: Department of Aeronautics and Astronautics, University of Washington, Seattle, WA 98195. Electronic mail: rzhu83ac@gmail.com.
[b)]Author to whom correspondence should be addressed. Also at: Institute of Engineering Mechanics, Beijing Jiaotong University, Beijing, People's Republic of China. Electronic mail: huangg@missouri.edu

intensively as for EM and acoustic waves. Zhou *et al.*[28] proposed a solid phononic crystal superlens capable of producing both negative refraction to focus propagating elastic waves and surface states to amplify evanescent waves. Lee *et al.*[29] designed an elastic plate hyperlens with alternating layers of aluminum and air which exhibited very strong anisotropy in elastic stiffness and produces an elliptical EFC. Oh *et al.*[30] experimentally demonstrated subwavelength imaging for elastic waves with a lens exhibiting hyperbolic EFC which results from the different deformation mechanisms along the two principal directions of the coiling-up microstructure in the unit cell. However, few research about elastic hyperlens design based on subwavelength-scale EMM with anisotropic mass density has been reported. Unlike anisotropic dynamic mass density in acoustic metamaterials, anisotropic mass density in EMMs can only be engineered by using anisotropic LR inclusions. Milton and Willis[20] first proposed a two-dimensional (2-D) spring-mass LR model which shows that the effective mass density could become anisotropic. Huang and Sun[21] systematically investigated the dynamic behavior of the 2-D LR mass-spring system and demonstrated that the effective mass density is actually a second-order tensor. Colquitt *et al.*[31,32] studied the dynamic anisotropy of lattice systems in vector problems of elasticity and the interaction of elastic waves with material with microstructure outside the standard homogenization regime. Antonakakis *et al.*[33] developed a continuum model for EMMs at high frequency range beyond long wavelength regime. Zhu *et al.*[22] proposed and experimentally validated a solid microstructure design of a continuum anisotropic EMM with complex resonant inclusions embedded in a solid plate which exhibited strong anisotropic mass density.

In this paper, we propose a novel microstructure design of a single-phase EMM with anisotropic dynamic mass density. The anisotropy of the effective mass density is caused by the decoupled resonant motions along the two principal in-plane directions. Single-phase microstructure design provides manufacturing feasibility particularly for plate-like structures. Effective material properties of the proposed EMM are calculated based on the numerical-based effective medium method and the hyperbolic EFCs of the EMM are obtained through the analytical derivation of wave propagation in the effective elastic medium with anisotropic mass densities. For practical applications, shunted piezoelectric elements are integrated into the microstructure to tune the effective mass density in a broad frequency range. Finally, an elastic hyperlens for a longitudinal elastic wave is demonstrated and super-resolution phenomenon ($\lambda/3$) is observed numerically.

II. MICROSTRUCTURAL DESIGN OF THE SINGLE-PHASE HYPERBOLIC EMM WITH ANISOTROPIC MASS DENSITY

Here, we present the first physical realization of a single-phase EMM plate which can manipulate LR motions along the two principal in-plane directions independently, as shown in Fig. 1. The thickness (z-direction) of the EMM plate is t. Two decoupled resonators, in-plane horizontal (x-direction) and in-plane vertical (y-direction), are proposed in the single-phase EMM unit cell. Therefore, negative effective mass densities of the EMM along the two principal directions can be expected in specified frequency ranges. The in-plane lattice constant of the square unit cell is a and the width of the slots is s. In the unit cell, two horizontal ribs with length r_h and width b_h are for the vertical resonator while one vertical rib with length r_v and width b_v is for the horizontal resonator. R_1 and R_2 are the radius of the vertical and horizontal resonators, respectively. The uniqueness of the design is that the LR motions of the EMM along the two principal in-plane directions are fully decoupled and therefore, it is possible to tailor the LR frequencies independently which leads to anisotropy in the effective mass density.[19,20] In the current design, the LR frequencies of the metamaterial along the two principal directions are determined by the in-plane bending stiffness of the rib beams and their attached masses. Thanks to the single-phase microstructure design, it is very feasible to apply the proposed hyperbolic EMM design to thin plate structures with precision manufacturing techniques such as laser cutting or CNC machining.

To illustrate this idea clearly, effective material properties of the metamaterial in Fig. 1(a) with two in-plane resonators will be analyzed to reflect the interior physical wave phenomena. Due to the complex microstructure in the unit cell, the numerical-based effective medium method will be used to calculate the effective material properties of the proposed EMM.[22,34] In the finite element (FE) model, the applied local displacement on the boundary of the EMM unit cell can be represented as $u_\alpha = (u_\alpha^0 + E_{\alpha\beta})e^{i\omega t}$, where u_α^0 is a rigid translation and $E_{\alpha\beta}$ is the global strain. The effective medium parameters can then be numerically obtained by considering the boundary responses of the unit cell to the stimulation exerted by the elastic waves. Under the long-wavelength assumption, the global stress, strain, resultant force, and acceleration of the unit cell can be numerically calculated by averaging local quantities on the external boundary of the unit cell as

$$\Sigma_{\alpha\beta} = \frac{1}{V}\int_{\partial V}\sigma_{\alpha\gamma}x_\beta ds_\gamma, \quad E_{\alpha\beta} = \frac{1}{2V}\int_{\partial V}(u_\alpha ds_\beta + u_\beta ds_\alpha),$$
$$F_\alpha = \frac{1}{V}\int_{\partial V}\sigma_{\alpha\beta}ds_\beta, \quad \ddot{U}_\alpha = \frac{1}{V}\int_{\partial V}\ddot{u}_\alpha\, ds, \tag{1}$$

where $\Sigma_{\alpha\beta}$, F_α, and $\ddot{U}_\alpha$ are the global stress, resultant force and acceleration, respectively. $\sigma_{\alpha\beta}$, x_α, u_α, and $\ddot{u}_\alpha$ are the local

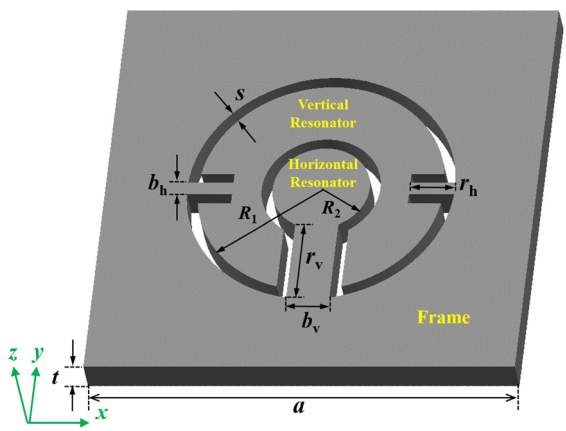

FIG. 1. (Color online) Unit cell design of the proposed single-phase EMM.

stress, position vector, displacement and acceleration fields, respectively. Specifically, the anisotropic effective mass density of the single-phase EMM along the x and y principal directions can be determined based on the following relation:

$$\begin{bmatrix} F_x \\ F_y \end{bmatrix} = -\omega^2 V \begin{bmatrix} \rho_{xx} & 0 \\ 0 & \rho_{yy} \end{bmatrix} \begin{bmatrix} U_x \\ U_y \end{bmatrix}, \tag{2}$$

where U_x and U_y are the global displacement fields along the x and y directions, respectively. V denotes the volume of the unit cell. As an example, the dynamic anisotropic mass densities of the EMM along the x and y in-plane principal directions as functions of frequencies are plotted as a solid curve and a dash curve in Fig. 2(a), respectively. Due to the very small thickness of the EMM plate, 2-D FE simulation with plane stress assumption is a good approximation and a computational efficient approach for the EMM analysis. In the figure, the effective mass densities are normalized with the average static mass density of the unit cell. The unit cell's geometric and material properties used in the calculation are listed in Table I.

As shown in Fig. 2(a), obvious differences between the values of ρ_{xx}^{eff} and ρ_{yy}^{eff} can be found after $f = 10$ kHz, which is due to the different LR frequencies of the unit cell along x and y directions being $f_x^{\text{LR}} = 15.23$ kHz and $f_y^{\text{LR}} = 15.8$ kHz, respectively, as shown in the zoom-in Fig. 2(b). The mode shapes at these two resonant frequencies are also demonstrated in Fig. 2(b) where the independent in-plane resonant motions of the horizontal and vertical resonators can be observed. Furthermore, different signs for ρ_{xx}^{eff} and ρ_{yy}^{eff} can be observed in two frequency ranges (15.23, 15.6 kHz) and (15.8, 17.25 kHz). Negative ρ_{xx}^{eff} and positive ρ_{yy}^{eff} is found in the first of the two frequency ranges while the opposite case is observed in the second range. The EMM with positive and negative mass densities along different in-plane principal directions in those frequency ranges could have hyperbolic dispersion curves and therefore, can be used for elastic hyperlens. The effective Young's and shear modulus of the single-phase EMM can also be calculated based on the effective model,[34] which on the contrary are almost constant values of $E_{\text{eff}} = 104$ GPa and $\nu_{\text{eff}} = 0.285$, respectively.

To characterize in-plane wave propagation in the plate-like EMM with anisotropic mass densities, the in-plane dispersion relations are derived based on the calculated effective material properties. The equations of motion for a

TABLE I. Unit cell geometrical and material parameters of the EMM.

Geometrical properties (in mm)		Material properties (stainless steel)	
s	0.5	Mass density	7850 kg/m^3
r_{h}	2.1	Young's modulus	200 GPa
r_{v}	4.1	Poisson's ratio	0.3
b_{h}	0.65		
b_{v}	2		
R_1	5.7		
R_2	2.25		
a	20		
t	1.5		

2-D homogenized medium with the anisotropic mass density tensor can be written as

$$\overline{\overline{\rho}} \frac{\partial^2 \overline{u}}{\partial t^2} = (M - G)\nabla\nabla \cdot \overline{u} + G\nabla^2 \overline{u}, \tag{3}$$

where $\overline{\overline{\rho}}$ is the anisotropic mass density tensor; $\overline{u}$ is the displacement vector; M and G are the effective P-wave modulus and effective shear modulus of the EMM, respectively. In order to separate the longitudinal and transverse wave modes, the displacement vector is expressed via Helmholtz decomposition as the gradient of a scalar and the curl of a zero divergence vector:[35]

$$\overline{u} = \nabla\Phi + \nabla \times \overline{H}, \qquad \nabla \cdot \overline{H} = 0, \tag{4}$$

where Φ and $\overline{H}$ are scalar and vector potentials, respectively. Then, the equations of motion in Eq. (3) can be rewritten as

$$\begin{aligned} \overline{\overline{\rho}} \left(\nabla \frac{\partial^2 \Phi}{\partial t^2} + \nabla \times \frac{\partial^2 \overline{H}}{\partial t^2} \right) &= (M - G)\nabla\nabla \\ &\quad \cdot (\nabla\Phi + \nabla \times \overline{H}) \\ &\quad + G\nabla^2(\nabla\Phi + \nabla \times \overline{H}). \end{aligned} \tag{5}$$

By conducting simplified tensor and vector operations, longitudinal and transverse wave equations of the motion can be separated as

$$\overline{\overline{\rho}} \nabla \frac{\partial^2 \Phi}{\partial t^2} - \nabla(M\nabla^2\Phi) = 0, \tag{6a}$$

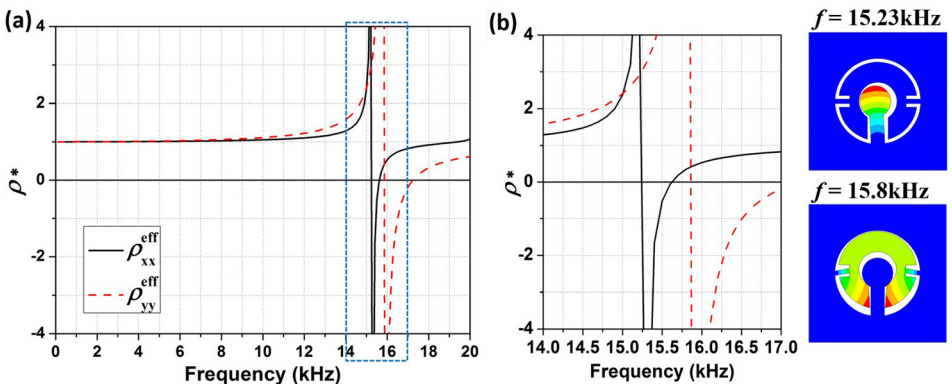

FIG. 2. (a) (Color online) Anisotropic effective mass density of the proposed single-phase EMM. (b) Zoom-in figure at the resonant frequency range and the two resonant modes at 15.23 and 15.8 kHz.

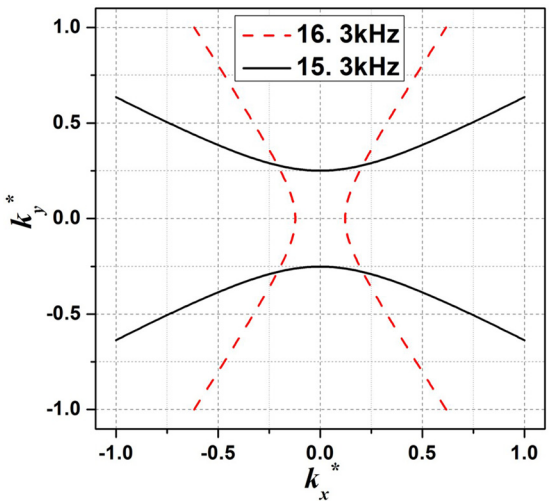

FIG. 3. (Color online) EFC of the proposed single-phase EMM calculated at $f = 15.3$ kHz and $f = 16.3$ kHz.

$$\overline{\overline{\rho}}\nabla \times \frac{\partial^2 \overline{H}}{\partial t^2} - G\nabla^2(\nabla \times \overline{H}) = 0. \tag{6b}$$

In this study, we focus on the longitudinal wave propagation in the medium with anisotropic mass densities. Therefore, after multiplying the reciprocal mass density tensor, $(\overline{\overline{\rho}})^{-1}$ and taking the divergence, $\nabla \cdot (*)$, to Eq. (6a), we obtain the following relation:

$$\frac{\partial^2(\nabla^2\Phi)}{\partial t^2} - \nabla \cdot \left[(\overline{\overline{\rho}})^{-1}\nabla(M\nabla^2\Phi)\right] = 0. \tag{7}$$

Since the x and y axes are the two principal directions of the EMM, only diagonal elements of the anisotropic mass density tensor and its reciprocal tensor remain as $\overline{\overline{\rho}} = \begin{bmatrix} \rho_{xx}^{\text{eff}} & 0 \\ 0 & \rho_{yy}^{\text{eff}} \end{bmatrix}$ and $(\overline{\overline{\rho}})^{-1} = \begin{bmatrix} 1/\rho_{xx}^{\text{eff}} & 0 \\ 0 & 1/\rho_{yy}^{\text{eff}} \end{bmatrix}$, respectively. Therefore, Eq. (7) can be rewritten as

$$\frac{M}{\rho_{xx}^{\text{eff}}}\frac{\partial^2(\nabla^2\Phi)}{\partial x^2} + \frac{M}{\rho_{yy}^{\text{eff}}}\frac{\partial^2(\nabla^2\Phi)}{\partial y^2} = \frac{\partial^2(\nabla^2\Phi)}{\partial t^2}. \tag{8}$$

By assuming the longitudinal plane wave with $\Phi = \Phi_0 \exp(-i\overline{k}^p \cdot \overline{r} - i\omega t)$, where $\overline{k}^p$ and $\overline{r}$ are the longitudinal wave vector and displacement vector, respectively, Eq. (8) can be rewritten as

$$\frac{(k_{xx}^p)^2}{\rho_{xx}^{\text{eff}}} + \frac{(k_{yy}^p)^2}{\rho_{yy}^{\text{eff}}} = \frac{\omega^2}{M}, \tag{9}$$

where k_{xx}^p and k_{yy}^p are the longitudinal wave vector components along the x and y principal directions, respectively. It can be found that the dispersion relation for the longitudinal wave propagating in the EMM with anisotropic mass density is the same as that for acoustic waves in anisotropic acoustic metamaterial.[36]

The equifrequency contours (EFCs) of the proposed single-phase EMM at $f = 15.3$ kHz and at $f = 16.3$ kHz are obtained by using Eq. (9), as shown in Fig. 3. The effective mass densities along the x and y principal directions at both frequencies can be obtained from Fig. 2 and the effective P-wave modulus M can be obtained based on the relation $M = K + (4/3)G$.

It can be seen in Fig. 3 that both EFCs demonstrate the hyperbolic shape as expected, which means the longitudinal elastic wave can propagate only along one principal direction where the effective mass density is positive and is forbidden in the other principal direction with negative effective mass density. In order to validate the anisotropic mass density and the directional wave propagation, the longitudinal wave fields inside a 2-D array of the proposed EMM unit cells at $f = 15.3$ kHz and $f = 16.3$ kHz are plotted in Figs. 4(a) and 4(b), respectively. The longitudinal waves are simulated by applying nodal forces normal to the circumference of a small circle positioned at the center of the array. A full-scale harmonic elastic wave simulation is performed using the commercial FE software COMSOL. The longitudinal wave field results are obtained by taking the divergence of the simulated displacement fields. Longitudinal wave propagating only along the y-axis is found at $f = 15.3$ kHz since the ρ_{xx}^{eff} is negative, as shown in Fig. 4(a) while longitudinal wave propagating only along the x axis is found at $f = 16.3$ kHz since the ρ_{yy}^{eff} becomes negative, as shown in Fig. 4(b). It is also observed that the wavelength in Fig. 4(a) is smaller than that in Fig. 4(b) because the positive ρ_{yy}^{eff} at $f = 15.3$ kHz is larger than the positive ρ_{xx}^{eff} at $f = 16.3$ kHz, which can be found in Fig. 2(b). The reflections in Fig. 4 are the result of the material mismatches between the EMM array and the surrounding steel medium.

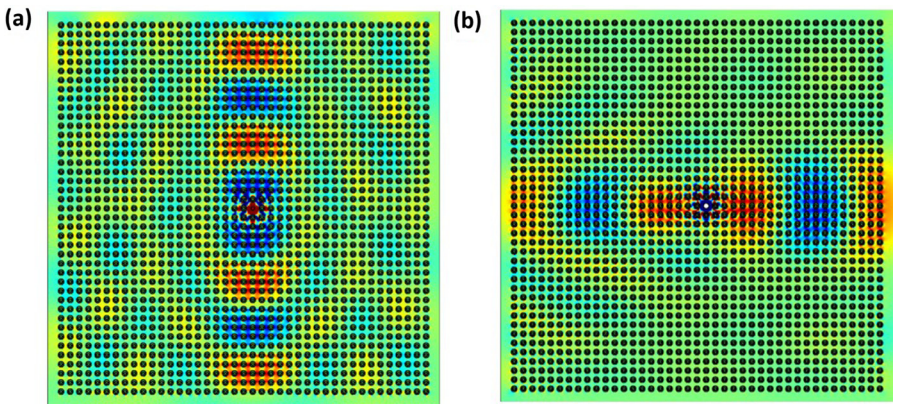

FIG. 4. (Color online) Longitudinal elastic wave propagations in the single-phase EMM at (a) $f = 15.3$ kHz and (b) $f = 16.3$ kHz.

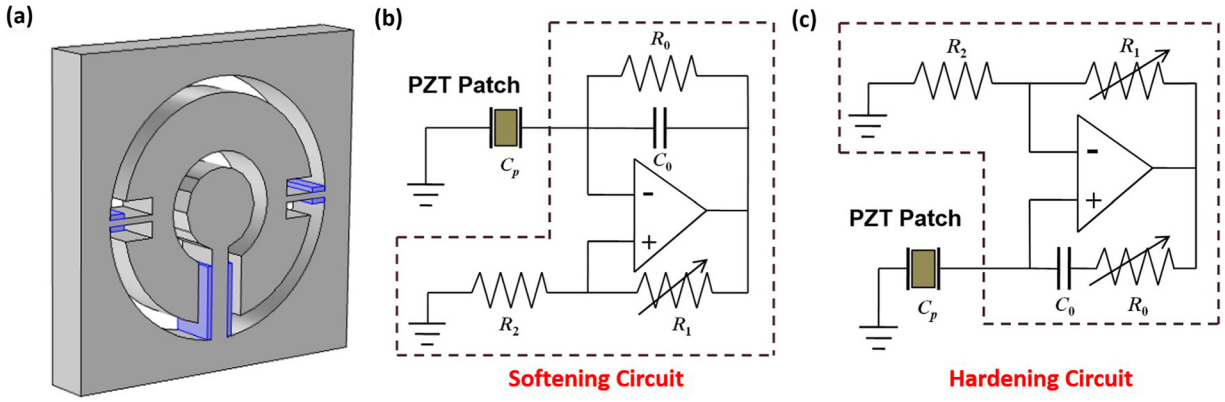

FIG. 5. (Color online) (a) Active unit cell design. (b) Softening circuit. (b) Hardening circuit.

III. ADAPTIVELY ELASTIC HYPERBOLIC METAMATERIAL

One of the major limitations of resonant-based EMMs as practical devices is that their operating frequency is fixed once the subwavelength-scale microstructures are fabricated. In order to overcome this limitation, "smart" components need to be integrated into the microstructures of the EMM. In this study, an adaptively hyperbolic EMM is proposed by employing piezoelectric patches shunted with negative capacitance (NC) into the microstructure to achieve tunable anisotropic mass density and therefore, the operation frequency range of the hyperbolic EMM can be greatly expanded. Figure 5(a) shows the microstructure design of the adaptive EMM by surface-bonding the shunted piezoelectric patches to the sides of the ribs. The geometric sizes of the piezoelectric patches attached to the horizontal and vertical ribs are $0.5\text{mm} \times 0.15\text{mm} \times 1.5\text{mm}$ and $0.15\text{mm} \times 2.25\text{mm} \times 1.5\text{mm}$, respectively. The geometric parameters of the unit cell as well as the material properties of the piezoelectric patches attached to the horizontal and vertical ribs are listed in Table II. Two types of NC circuits, namely, "softening" and "hardening" circuits, are used for the piezoelectric patches to actively increase or decrease the bending stiffness of the ribs and therefore, tune the LR frequencies of the unit cell along the two principal directions as shown in Figs. 5(b) and 5(c), respectively. In the figures, negative equivalent capacitances, C_N, can be obtained inside the dotted squares. C_p is the capacitance of the piezoelectric patch. The softening circuit consists of a capacitor C_0, a potentiometer R_1, two resistors R_0 and R_2 and an operational amplifier, which can be theoretically operated with the stability condition being $C_N > C_p$. In the hardening circuit, a resistor R_0 is replaced by a potentiometer in order to adjust the resistance and in which the stability condition should be satisfied as $C_N < C_p$. For both circuits, the negative equivalent capacitances, C_N, can be calculated as $C_N = -C_0(R_1/R_2)$.[37,38]

TABLE II. Geometric parameters of unit cell and material properties of the PZT patches.

Geometrical properties of the unit cell (in mm)		Material properties (PZT patch)	
s	0.5	Mass density	7500 kg/m^3
r_h	2.1	Young's modulus	72 GPa
r_v	2.75	Poisson's ratio	0.34
b_h	0.2		
b_v	0.6		
R_1	3.5		
R_2	1.25		
a	10		
t	1.5		

Figures 6(a) and 6(b) show the obtained effective mass densities along x and y principal directions, respectively. Three different configurations are simulated with the piezoelectric patch connecting to an open circuit, a softening circuit ($\lambda = -0.98$) and a hardening circuit ($\lambda = -1.03$), where the negative capacitance ratio (NCR) λ of the NC circuit is defined as $\lambda = C_N/C_p$. The effective anisotropic mass density can be calculated by using a multi-physics numerical-based effective medium model and the method is then implemented into COMSOL. As shown in Fig. 6(a), it can be found that the resonant peak of ρ^*_{xx} shifts to lower (dash curve) and higher (solid curve) frequencies when softening and harden circuits are connected to the vertical piezoelectric patches, respectively. The same phenomenon can be found for the resonant peak of ρ^*_{yy} when the softening and hardening circuits are connected to the horizontal piezoelectric patches. The tunability of the resonant frequency along the x and y principal directions are measured as 33.3% and 27.5%, respectively.

IV. ELASTIC HYPERLENS BY ANISOTROPIC METAMATERIALS

While the elastic lens having elliptic EFCs is capable of subwavelength imaging,[11,29] higher-resolution by the proposed hyperlens is apparent because finer subwavelength information can be carried considerably better so that the distance between the two sources can be reduced further. To illustrate the better performance of the lens having hyperbolic EFC, Fig. 7(a) shows the design of an elastic hyperlens consisting of 1403 single-phase anisotropic EMM unit cells. The proposed hyperlens spans 180° in the angular direction and has inner and outer radiuses of 240 and 640 mm, respectively. Along the radial direction, it consists of 20 layers of EMM unit cells and the distance between two neighboring

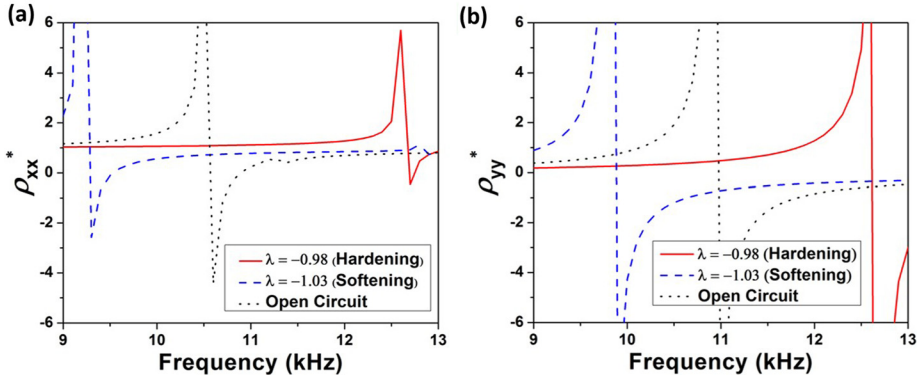

FIG. 6. (Color online) Effective mass densities of the active EMM along (a) x and (b) y directions.

layers of EMM unit cells is $a = 20$ mm which is the same as the distance between two neighboring unit cells along the circumferential direction. In order to demonstrate the subwavelength imaging ability of the proposed elastic hyperlens, full-scale harmonic elastic wave simulations using COMSOL are performed. The dimensions of the host medium made of steel ($\rho = 7850\,\text{kg/m}^3$, $E = 200$ GPa and $\upsilon = 0.3$) are 1600 mm × 1000 mm. Perfectly matched layers (PMLs), highlighted in Fig. 7(a), are applied to the boundaries of the simulation region to eliminate any unwanted reflections. Figures 7(b) and 7(c) show the zoomed-in pictures of the meshed hyperlens and the single-phase EMM unit cell, respectively. The simulation frequency is chosen at $f = 15.3$ kHz where the effective mass density is positive along the radial direction but negative along the angular direction as predicted in Fig. 2. As shown in Fig. 7(a), two omnidirectional longitudinal wave sources are simulated by applying nodal forces normal to the circumferences of two small circles which have a radius of only 2 mm and are separated by $(1/3)\lambda$, where λ is the wavelength of the longitudinal elastic wave in steel. The distance between the sources and the first layer of the EMM unit cells along the radial direction is 20 mm. The input waves from the two longitudinal wave sources are expected to enter the hyperlens region and be guided along the radial direction. The output wave field will be measured along a predefined curve which is parallel to the last layer of the hyperlens with the same distance of 20 mm between them. The predefined curve is highlighted, as shown in Fig. 7(a). Note that the studied longitudinal wave wavelength λ is much larger than the size of the single-phase EMM unit cell a at $\lambda = 18a$. To clearly explain hyperbolic wave dispersion mechanism, simulations are also performed on the hyperlens made of the homogeneous medium with the same geometric shape and effective mass densities along the radial and angular directions as $\rho_r = 23\,500\,\text{kg/m}^3$ and $\rho_\theta = -68\,600\,\text{kg/m}^3$, respectively, which are obtained from the results of the numerical-based effective medium model at 15.3 kHz.

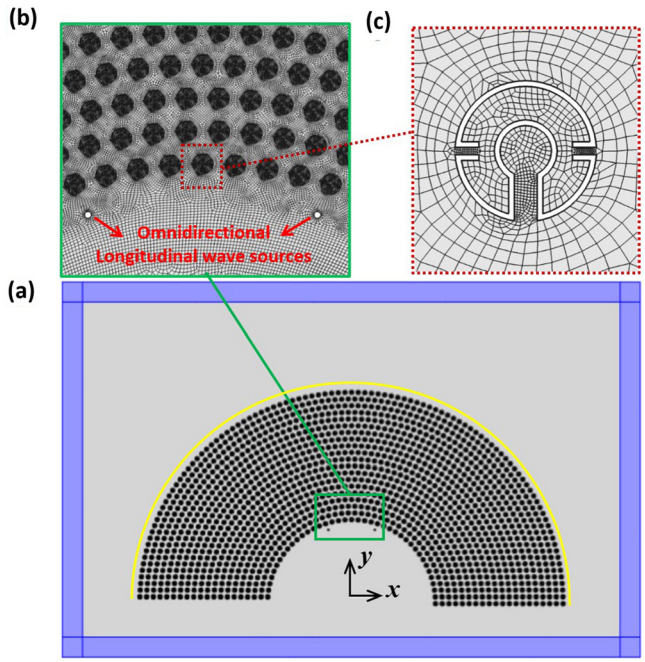

FIG. 7. (Color online) (a) Design of elastic hyperlens. (b) Zoom-in meshed hyperlens with two omnidirectional longitudinal wave sources. (c) Zoom-in meshed EMM unit cell.

The in-plane longitudinal and the transverse wave propagations in the hyperlenses with single-phase EMM are shown in Figs. 8(a) and 8(b), respectively. The divergence and curl of the simulated displacement fields are plotted to separate the longitudinal and transverse wave fields, respectively.[27] As shown in Fig. 8(a), the longitudinal waves propagate along the radial direction of the hyperlens and two separate wave propagation channels inside the hyperlens region can be clearly observed. At the outer boundary of the hyperlens, the distance between two sources is enlarged. Once the magnified feature is larger than the diffraction limit, then we can observe the subwavelength features of the object in the far field. In Fig. 8(b), weak transverse waves are generated at the interface between the hyperbolic EMM and the steel matrix near the wave sources due to the wave mode conversion. However, the transverse wavenumber along the radial direction of the hyperlens is an imaginary value due to the band gap of the shear wave mode which is generated by the negative effective mass density along the angular direction at 15.3 kHz,[21] and therefore the transverse wave cannot propagate along the radial direction, as shown in Fig. 8(b). It should be mentioned that the proposed anisotropic EMM could be also extended for the hyperlens design of the shear wave because propagations of both the longitudinal and shear waves can be controlled by independently adjustable effective mass densities along two principle directions. However, in order to do that, a hyperlens model for

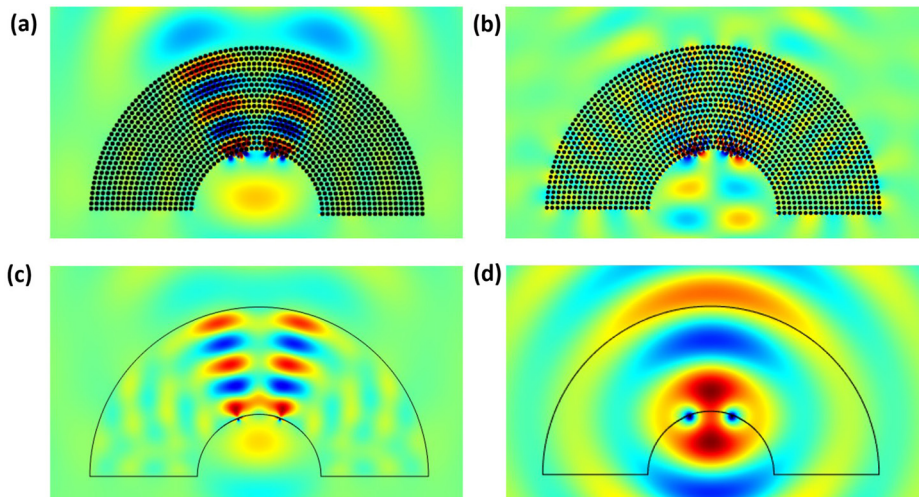

FIG. 8. (Color online) (a) The divergence of the displacement fields for hyperlens with single-phase EMM unit cells. (b) The curl of the displacement fields for hyperlens with single-phase EMM unit cells. (c) The divergence of the displacement fields for hyperlens with effective homogenous medium. (d) The divergence of the displacement fields without hyperlens.

the shear wave should be derived to determine required anisotropic mass densities, which is not the main objective in the current study and will be investigated in the future work.

The longitudinal wave propagation in the hyperlens with effective homogenous medium is shown in Fig. 8(c), where the effective Young's modulus and Poisson's ratio are $E_{\text{eff}} = 104$ GPa and $\upsilon_{\text{eff}} = 0.285$, respectively. In general, the simulation results of the hyperlens with the detailed microstructures is in agreement with the result of the hyperlens with effective medium. The minor difference in the intensity of the wave field of the hyperlens is due to fact that the effective mass density of the resonant-based metamaterial system is strongly dependent on the operating frequency, which is obtained under the assumption of the long wavelength frequency. Also, to illustrate the effects of the hyperlens, the longitudinal displacement field without a hyperlens (steel in the hyperlense region) is provided in Fig. 8(d) for reference. Comparing Fig. 8(a) with Fig. 8(d), compressed wave patterns can be found inside the EMM hyperlens, which is due to the large effective mass density and decreased effective longitudinal wave velocity along the radial direction in the EMM array. It is also noticed that the imaging quality of the single-phase elastic hyperlens is determined by the size of the microstructure compared with the wavelength in the incident plane, which can be further improved by downsizing the side length of the microstructure. However, difficulty will be increase for the metamaterial fabrication.

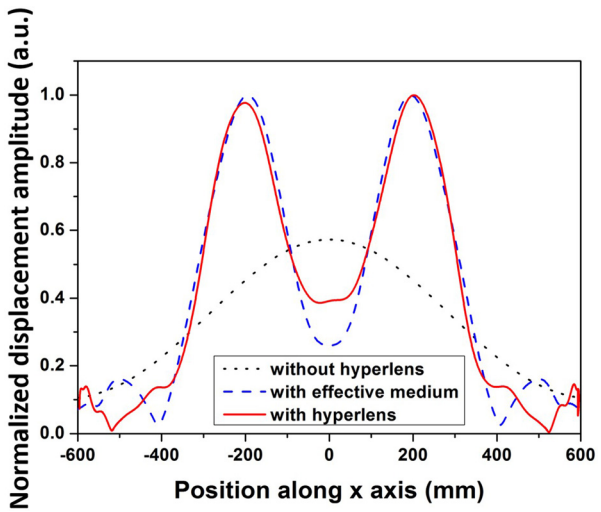

FIG. 9. (Color online) Imaging performances of with hyperlens case, with effective medium case and without hyperlens case.

Furthermore, the normalized displacement intensity distributions of the longitudinal waves obtained at the output curve after passing through the hyperlens region are plotted as a solid curve, a dash curve and a dot curve for with hyperlens case, with effective medium case and without hyperlens case, respectively, as shown in Fig. 9. The x-axis of the figure indicates the position of each measuring point on the output curve along the x-axis in Fig. 7(a). The normalizations in Fig. 9 were carried out by taking the amplitudes of the measured displacement fields divided by the maximum displacement amplitude measured along the output curve for hyperlens with single-phase EMM unit cells. Two peaks can be clearly observed for the case with hyperlens and the case with effective medium while only a single peak appears for the case without a hyperlens, which confirms the subwavelength imaging ability of the proposed elastic hyperlens for longitudinal elastic waves. It can also be observed that the maximum normalized transmittance reaches 0.98 at the imaging position with the hyperlens, while only 0.58 at the central position of the curve without the hyperlens owing to the intense diffractions occurring. It can be seen that the distance between two images is about 1.02λ at the outer boundary of the hyperlens with a magnification ratio of 3.06 and also larger than the diffraction limit 0.5λ. Thus, the subwavelength object is efficiently identified and magnified by the elastic hyperlens with a single-phase microstructure.

V. CONCLUSIONS

In this paper, a microstructure design of a single-phase EMM with anisotropic dynamic mass density is proposed. Anisotropic effective mass density in the EMM is realized by the decoupled resonant motions along the two principal directions and can have opposite signs. Effective material properties of the EMM are calculated by the numerical-based effective medium method and the hyperbolic dispersion relations are obtained. For application in a broad

frequency range, NC shunted piezoelectric patches are integrated into the microstructure and a tunable effective mass density is demonstrated. Finally, super-resolution phenomenon ($\lambda/3$) of a longitudinal elastic wave has been demonstrated numerically by using an elastic hyperlens made of the single-phase EMM. The proposed metamaterial could have many promising applications in high resolution damage imaging in nondestructive evaluation and structural health monitoring.

ACKNOWLEDGMENT

This work was supported by the Air Force Office of Scientific Research under Grant No. AF 9550-15-1-0061 with Program Manager Dr. Byung-Lip (Les) Lee.

[1]J. B. Pendry, "Negative refraction makes a perfect lens," Phys. Rev. Lett. **85**, 3966 (2000).
[2]Z. Jacob, L. V. Alekseyev, and E. Narimanov, "Optical hyperlens: Far-field imaging beyond the diffraction limit," Opt. Express **14**, 8247–8256 (2006).
[3]M. Ambati, N. Fang, C. Sun, and X. Zhang, "Surface resonant states and superlensing in acoustic metamaterials," Phys. Rev. B **75**, 195447 (2007).
[4]H. Jia, M. Ke, R. Hao, Y. Ye, F. Liu, and Z. Liu, "Subwavelength imaging by a simple planar acoustic superlens," Appl. Phys. Lett. **97**, 173507 (2010).
[5]J. Zhu, J. Christensen, J. Jung, L. Martin-Moreno, X. Yin, L. Fok, X. Zhang, and F. J. Garcia-Vidal, "A holey-structured metamaterial for acoustic deep-subwavelength imaging," Nat. Phys. **7**, 52–55 (2011).
[6]X. Zhou and G. Hu, "Superlensing effect of an anisotropic metamaterial slab with near-zero dynamic mass," Appl. Phys. Lett. **98**, 263510 (2011).
[7]A. Liu, X. Zhou, G. Huang, and G. Hu, "Super-resolution imaging by resonant tunneling in anisotropic acoustic metamaterials," J. Acoust. Soc. Am. **132**, 2800–2806 (2012).
[8]N. Kaina, F. Lemoult, M. Fink, and G. Lerosey, "Negative refractive index and acoustic superlens from multiple scattering in single negative metamaterials," Nature **525**, 77–81 (2015).
[9]J. Christensen and F. J. Garcia de Abajo, "Anisotropic metamaterials for full control of acoustic waves," Phys. Rev. Lett. **108**, 124301 (2012).
[10]V. M. Garcia-Chocano, J. Christensen, and J. Sánchez-Dehesa, "Negative refraction and energy funneling by hyperbolic materials: An experimental demonstration in acoustics," Phys. Rev Lett. **112**, 144301 (2014).
[11]J. Li, L. Fok, X. Yin, G. Bartal, and X. Zhang, "Experimental demonstration of an acoustic magnifying hyperlens," Nat. Mater. **8**, 931–934 (2009).
[12]C. Shen, Y. Xie, N. Sui, W. Wang, S. A. Cummer, and Y. Jing, "Broadband acoustic hyperbolic metamaterial," Phys. Rev. Lett. **115**, 254301 (2015).
[13]X. Ao and C. T. Chan, "Far-field image magnification for acoustic waves using anisotropic acoustic metamaterials," Phys. Rev. E **77**, 025601 (2008).
[14]T. Chiang, L. Wu, C. Tsai, and L. Chen, "A multilayered acoustic hyperlens with acoustic metamaterials," Appl. Phys. A **103**, 355–359 (2011).
[15]D. Lu and Z. Liu, "Hyperlenses and metalenses for far-field super-resolution imaging," Nat. Commun. **3**, 1205 (2012).
[16]Z. Liu, X. Zhang, Y. Mao, Y. Y. Zhu, Z. Yang, C. T. Chan, and P. Sheng, "Locally resonant sonic materials," Science **289**, 1734–1736 (2000).
[17]H. H. Huang, C. T. Sun, and G. L. Huang, "On the negative effective mass density in acoustic metamaterials," Int. J. Eng. Sci. **47**, 610–617 (2009).
[18]X. M. Zhou and G. K. Hu, "Analytic model of elastic metamaterials with local resonances," Phys. Rev. B **79**, 195109 (2009).
[19]N. Fang, D. Xi, J. Xu, M. Ambati, W. Srituravanich, C. Sun, and X. Zhang, "Ultrasonic metamaterials with negative modulus," Nat. Mater. **5**, 452–456 (2006).
[20]G. W. Milton and J. R. Willis, "On modifications of Newton's second law and linear continuum elastodynamics," Proc. R. Soc. A **463**, 855–880 (2007).
[21]H. H. Huang and C. T. Sun, "Locally resonant acoustic metamaterials with 2D anisotropic effective mass density," Philos. Mag. **91**, 981–996 (2011).
[22]R. Zhu, X. N. Liu, G. L. Huang, H. H. Huang, and C. T. Sun, "Microstructural design and experimental validation of elastic metamaterial plates with anisotropic mass density," Phys. Rev. B **86**, 144307 (2012).
[23]T. Bückmann, M. Kadic, R. Schittny, and M. Wegener, "Mechanical metamaterials with anisotropic and negative effective mass-density tensor made from one constituent material," Phys. Status Solidi B **252**, 1671–1674 (2015).
[24]X. Yan, R. Zhu, G. L. Huang, and F. G. Yuan, "Focusing guided waves using surface bonded elastic metamaterials," Appl. Phys. Lett. **103**, 121901 (2013).
[25]Y. Y. Chen, J. Hu, and G. L. Huang, "A design of active elastic metamaterials for control of flexural waves using the transformation method," J. Intell. Mater. Syst. Struct. (2015).
[26]X. N. Liu, G. K. Hu, G. L. Huang, and C. T. Sun, "An elastic metamaterial with simultaneously negative mass density and bulk modulus," Appl. Phys. Lett. **98**, 251907 (2011).
[27]R. Zhu, X. N. Liu, G. K. Hu, G. L. Huang, and C. T. Sun, "Negative refraction of elastic waves at the deep-subwavelength scale in a single-phase metamaterial," Nat. Commun. **5**, 5510 (2014).
[28]X. M. Zhou, M. B. Assouar, and M. Oudich, "Acoustic superfocusing by solid phononic crystals," Appl. Phys. Lett. **105**, 233506 (2014).
[29]H. J. Lee, H. W. Kim, and Y. Y. Kim, "Far-field subwavelength imaging for ultrasonic elastic waves in a plate using an elastic hyperlens," Appl. Phys. Lett. **98**, 241912 (2011).
[30]J. H. Oh, H. M. Seung, and Y. Y. Kim, "A truly hyperbolic elastic metamaterial lens," Appl. Phys. Lett. **104**, 073503 (2014).
[31]D. J. Colquitt, I. S. Jones, N. V. Movchan, A. B. Movchan, and R. C. McPhedran, "Dynamic anisotropy and localization in elastic lattice systems," Waves Random Complex Media **22**, 143–159 (2012).
[32]D. J. Colquitt, I. S. Jones, N. V. Movchan, and A. B. Movchan, "Dispersion and localization of elastic waves in materials with microstructure," Proc. R. Soc. London A **467**, 2874–2895 (2011).
[33]T. Antonakakis, R. V. Craster, and S. Guenneau, "Homogenization for elastic photonic crystals and dynamic anisotropy," J. Mech. Phys. Solids **71**, 84–96 (2014).
[34]X. N. Liu, G. K. Hu, C. T. Sun, and G. L. Huang, "Wave propagation characterization and design of two-dimensional elastic chiral metacomposite," J. Sound Vib. **330**, 2536–2553 (2011).
[35]J. L. Rose, *Ultrasonic Waves in Solid Media* (Cambridge University Press, New York, 1999), pp. 24–39.
[36]D. Torrent and J. Sanchez-Dehesa, "Acoustic metamaterial for new two-dimensional sonic device," New J. Phys. **9**, 323 (2007).
[37]Y. Y. Chen, G. L. Huang, and C. T. Sun, "Band gap control in an active elastic metamaterial with negative capacitance piezoelectric shunting," ASME J. Vib. Acoust. **136**, 061008 (2014).
[38]R. Zhu, Y. Y. Chen, M. V. Barnhart, G. K. Hu, C. T. Sun, and G. L. Huang, "Experimental study of an adaptive elastic metamaterial controlled by electric circuits," Appl. Phys. Lett. **108**, 011905 (2016).